Observation of flaking process in rolling contact fatigue of bearing steel with spheroidal inclusions by laminography using ultrabright synchrotron radiation X-rays

Nakai, Yoshikazu ; Shiozawa, Daiki ; Kikuchi, Shoichi ; Nishina, Takashi ; Kobayashi, Hiroshi ; Kurahashi, Masanori ; Makino, Taizo ;…

(Citation)
Fatigue & Fracture of Engineering Materials & Structures,46(12):4541-4557

(Issue Date)
2023-12

(Resource Type)
journal article

(Version)
Accepted Manuscript

Observation of Flaking Process in Rolling Contact Fatigue of Bearing Steel with Spheroidal Inclusions by Laminography Using Ultrabright Synchrotron Radiation X-rays

Yoshikazu Nakai* and Daiki Shiozawa
Department of Mechanical Engineering, Kobe University
1-1, Rokkodai, Nada, Kobe 657-8501, Japan
* Corresponding author, nakai@mech.kobe-u.ac.jp

Shoichi Kikuchi
Department of Mechanical Engineering, Shizuoka University
3-5-1, Johoku, Naka, Hamamatsu 432-8561, Japan

Takashi Nishina, Hiroshi Kobayashi, and Masanori Kurahashi
Department of Mechanical Engineering, Kobe University
1-1, Rokkodai, Nada, Kobe 657-8501, Japan

Taizo Makino
Nippon Steel Corporation, Research & Development, 1-8, Fuso, Amagasaki 660-0891, Japan

Yutaka Neishi
Nippon Steel Corporation, Research & Development, 20-1 Shintomi, Futtsu 293-8511, Japan

Key words: Rolling contact fatigue; Crack path; Image processing; Inclusions

Shiozawa shiozawa@mech.kobe-u.ac.jp
Kikuchi kikuchi.shoichi@shizuoka.ac.jp
Nishina t.n.247@ezweb.ne.jp
Kobayashi hiroshi.kobayashi.hiroshi@gmail.com
Kurahashi 0ba65k2538v599t@ezweb.ne.jp
Makino makino.hb3.taizo@jp.nipponsteel.com
Neishi neishi.58e.yutaka@jp.nipponsteel.com

Abstract

Rolling contact fatigue tests were performed on specimens containing spheroidal inclusions to clarify the effect of the orientation of inclusions, and the results were compared with those of specimens containing stringer-shaped inclusions. For all types of inclusion, cracks first formed on the rolling surface and then propagated in the depth direction, and an internal crack parallel to the rolling surface formed from the deepest point of the vertical crack, which led to flaking. The flaking life of the specimens with spheroidal inclusions was longer than that of the specimens with stringer-shaped inclusions, where the initiation and propagation live of cracks were affected by the inclusion shape and size. The surface crack initiation life was shorter for specimens with longer surface inclusions, whereas the crack propagation life decreased with the depth of surface inclusion. The greater the scatter of the size of inclusions, the greater the scatter of flaking life.

1. INTRODUCTION

Longer service life and mass reduction of machinery are important issues for solving resource and energy problems. The contribution of mass reduction due to higher strength and lengthening of life of mechanical elements used in transportation machinery, such as bearings, gears, wheels, and rails, is particularly significant. For this purpose, it is important to elucidate the mechanism underlying rolling contact fatigue (RCF), which can be divided into two types.[1,2] One type occurs in gears, wheels, and rails where strong friction (tangential force) occurs on the rolling contact surfaces. In this case, macroslip plays an important role in the damage process, where cracks initiate on the surface and then propagate diagonally from the surface to the interior, eventually generating damage known as shelling or pitting.[2,3] The other type of damage occurs in machine parts used under pure rolling contact or oil lubrication owing to weak friction without macroslip, as in bearings. In this case, it has been considered that cracks occur in the interior under the contact surface, where the maximum shear stress acts, causing damage called flaking.[4-7] The above-described difference was attributed to the stress intensity factor range of cracks below the surface,[8] or shear stress distribution.[9] Not only the initiation site, but also the initiation mechanism of cracks differs in RCF between strong and weak friction, *i.e.*, shelling/pitting and flaking.[4] The mechanics of shelling/pitting was analyzed on the basis of fracture mechanics[1,10,11] and on the basis of shear stress calculated by finite element (FE) analysis.[12–14] Since the purpose of this study is to elucidate the mechanisms of RCF initiation and propagation in bearings, the term RCF will be used hereafter exclusively for damage caused by weak friction.

In RCF, microstructural alternation of the matrix under the surface is an important cause of RCF without friction under oil lubrication.[11-27] Such alterations may be a dark etching area (DEA),[15,16] dark etching constituent (DEC),[15] dark etching region (DER),[15,17] and martensite transformation from retained austenite,[16,21] which occur in high-stress regions under the raceway. As the number of fatigue

cycles increases, characteristic microstructures appear, such as the white band (WB),[15,16] which is type a of shear band, the white etching band (WEB),[15,17] white etching area (WEA),[15, 18–24] white etching cracks (WEC),[17,19] brown etching layer (BEL),[18] and butterfly cracks.[20] The WEA was found to be composed of ultrafine nanocrystalline ferrite grains, voids, and spherical carbides, as observed by transmission electron microscopy.[19–23] Hiraoka et al.[5] observed that WEA occurred after microcrack initiation. Martin et al.[25] examined microstructural alterations, which develop with cyclic stressing under rolling contact, and attempted to define their nature and formation mechanisms. In many cases, 'winglike' structural alterations, commonly called 'butterflies', were microcracks associated with inclusions.[24,26,27] Evans et al.[20] conducted 3D reconstruction of the butterfly wing by cross-sectional focused ion beam (FIB) milling with an average slice thickness of 350 nm.

Whereas numerous studies have been conducted on microstructural alterations, the process from microstructural alternation to flaking has not been clarified, and its relationship with the life and strength of RCF is unknown. On the other hand, in RCF, Kanetani and Ushida reported that cracking starts from nonmetallic inclusions rather than WBs.[15] The detrimental effect of inclusions in terms of RCF has been discussed,[5-7,20,24,28-42] and it has been found that the size, shape, orientation, and position of the inclusions and the interface state between the inclusions and the surrounding matrix affect the RCF life,[5-7,24,28-33,35,40,41] and that the miniaturization of the inclusions contributes to the strength improvement of RCF.[33] It has also been reported that the type of inclusion also affects crack initiation in RCF. Oxide inclusions are known to be detrimental to RCF life, and many studies have been conducted to clarify the effects of oxide size, oxide composition,[35] and matrix–oxide interface state on RCF life.[30] Previous results have shown that the RCF life can be improved by reducing the oxide size and interface cavities, and by tuning the oxide chemical composition. Indeed, the RCF life was extended as a result of reducing the total oxygen content in the bearing steel by improving the manufacturing process.

On the other hand, reducing the number of oxide inclusions in steel has caused the effect of other inclusions, such as MnS, to be greater than that of oxide inclusions.[35] Since MnS inclusion is deformable, its shape can be controlled. To ensure excellent RCF life, it is necessary to clarify the effect of MnS inclusion shape to improve RCF strength; however, there are only a few studies on the effect of MnS shape on RCF life. Therefore, in the present study, we focus on the effect of inclusion shape on RCF life.

Alley and Neu[43] analyzed the effect of the orientation on lateral inclusions. Their analysis was based on the stress beneath the surface, which was calculated by FE analysis. They found that RCF strength is lowest for inclusions with the orientation of 45º, where the orientation is defined as the complementary angle between the long axis of an inclusion and the normal of the surface, and the RCF strength is highest for the orientation of 0º (vertical inclusion). On the other hand, Allison and Pandkar[44] evaluated the RCF limit of longitudinal and lateral inclusions using the maximum

orthogonal shear stress beneath the surface calculated by FE analysis, and concluded that the effects of the inclusion orientation and geometry on the RCF limit were minor.

Another subject concerning RCF is the failure probability, because the basic rating life of bearings, L_{10} is defined as the rating life in million revolutions of bearings where 90% of bearings do not fail under identical loading and lubrication conditions. Using the orthogonal shear stress calculated by FE analysis and using the *S–N* curve obtained by the conventional fatigue test, the various research groups evaluated fracture probability in RCF, where the scatter of RCF life values attributed to the scatter in the conventional fatigue test[45–48] or crystalline anisotropy.[49] Kerrigan et al.[31] and Unigame[32] reported that the inclusion distribution obtained from the statistics of extreme values can be used to predict L_{10} life.

As mentioned above, in previous studies on RCF, it has been considered that RCF originates from subsurface inclusions where the shear stress under the contact surface is maximum and cracks grow from there toward the surface[6,7]; however, the RCF process has been observed destructively by cutting specimens because it is not possible to observe cracks inside the specimens at high magnification.[50,51] Therefore, it has been difficult to sequentially observe the RCF process. On the other hand, three-dimensional imaging of cracks in steel with submicron resolution by computed tomography using ultrabright synchrotron radiation X-rays (SR-μCT) have succeeded.[42,52-54] We also observed microstructural alternations related to fatigue crack initiation by diffraction contrast tomography (DCT) using ultrabright synchrotron radiation X-rays.[55,56]

We first performed RCF tests on specimens with EDM-machined circular holes simulating stringer-shaped inclusions of various diameters and depths, and we then observed the crack initiation morphology by SR-μCT of the specimens cut out including the holes.[28] Next, the RCF test was interrupted and laminography, which is used to observe crack initiation and propagation behavior sequentially, was performed using ultrabright synchrotron radiation X-rays.[57-62] The results of RCF tests on plate specimens containing stringer-shaped MnS inclusions revealed that the cracks originated from inclusions on the specimen surface and propagated into the interior, forming additional cracks parallel to the surface from around the tips of the original cracks, rather than

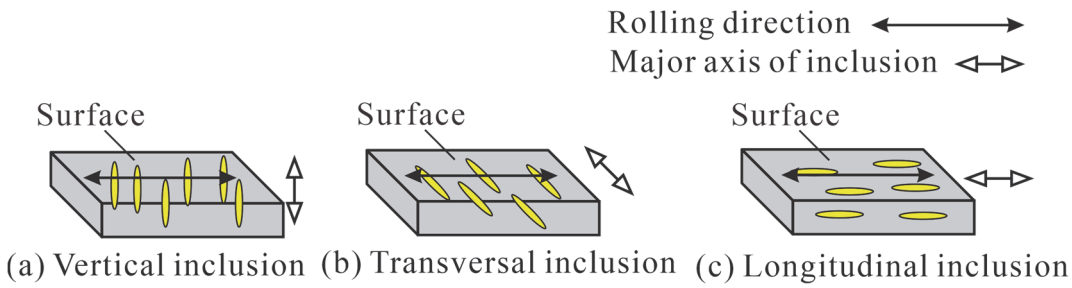

FIGURE 1 Orientation of inclusions in specimens. (a) the major axis of inclusion is perpendicular to the surface and perpendicular to the rolling direction, (b) the major axis of inclusion is parallel to the surface and perpendicular to the rolling direction, and (c) the major axis of inclusion is parallel to the surface and parallel to the rolling direction.

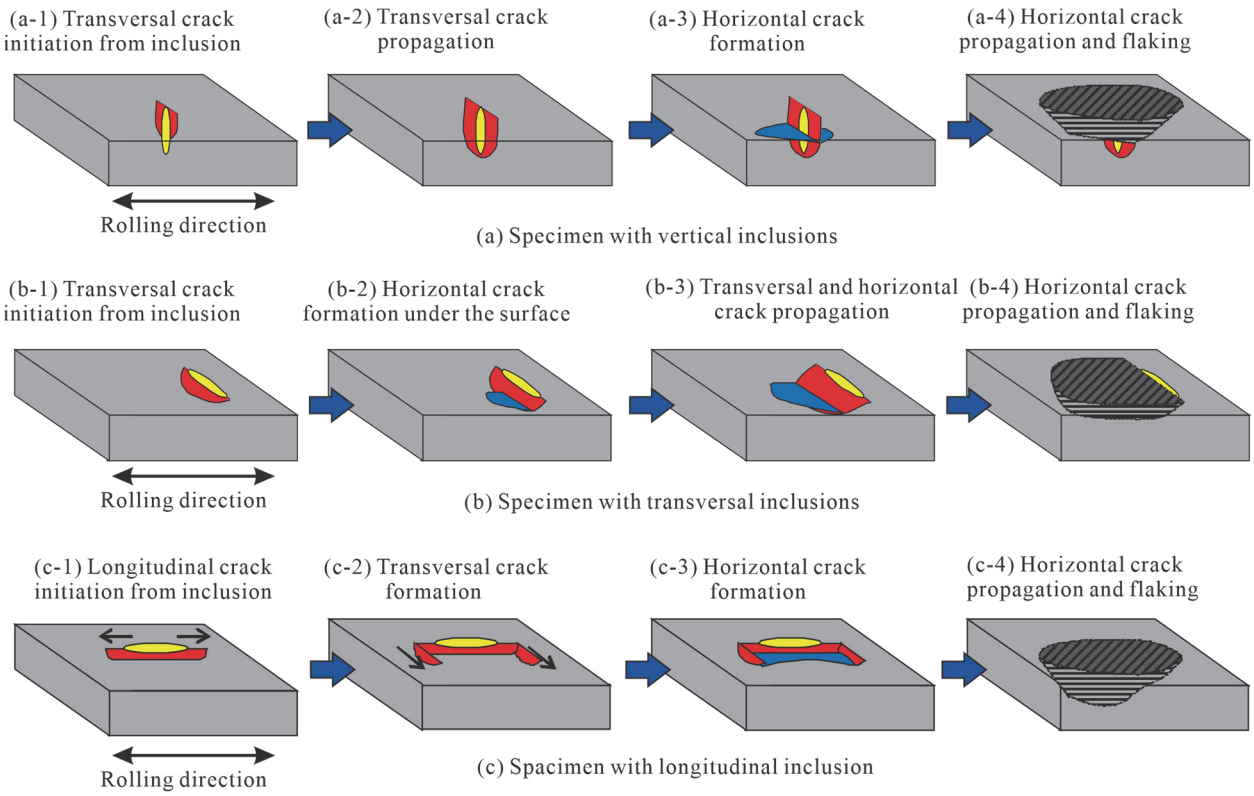

FIGURE 2 Flaking mechanism for stringer-shaped inclusions, where yellow regions show inclusions, red regions show cracks vertical cracks and blue regions show horizontal cracks.[62]

propagating from the interior toward the surface and forming flaking, as previously believed.

We also examined the effect of stringer-type inclusion orientation relative to the rolling direction, as shown in Figure 1[62,] and found that the flaking formation process for stringer-shaped inclusions, which differs depending on the orientation of the inclusion relative to the rolling direction as shown in Figure 2.[41,62] In the case of specimens with inclusions whose longitudinal direction is perpendicular to the rolling direction (lateral inclusions), as shown in Figures 2a and 2b, cracks perpendicular to the rolling direction formed on the surface, which propagated in the internal direction, and cracks parallel to the specimen surface started to form near its deepest point, resulting in flaking. In the case of a specimen containing a longitudinal inclusion whose longitudinal direction is parallel to the rolling direction (longitudinal inclusion), as shown in Figure 2c, the crack started at the long end of the inclusion, propagated a certain distance in the rolling direction, and then kinked in the direction perpendicular to the rolling direction. The subsequent behavior after the kinking was similar to that of the specimens containing lateral inclusions. This difference in crack initiation and propagation behavior can be explained by the time variation with the rolling of the antiplane shear stress at the crack initiation point.

In this study, RCF tests were conducted on specimens with spheroidal MnS inclusions to observe crack initiation and propagation behavior. The average and scatter of flaking life were analyzed on the basis of Weibull plots, and results were compared with those of stringer-shaped inclusions

Table 1. Density and sizes of inclusions.

Inclusion type	Density ($1/mm^3$)	Mean volume (μm^3)	Length in radial direction (μm)		Length in forged direction (μm)		Aspect ratio
			Mean	Standard deviation	Mean	Standard deviation	
Spheroidal	4.22×10^4	171	8.42	2.92	11.80	7.25	1.4
Stringer	1.16×10^4	489	8.91	3.98	20.9	15.5	2.34

reported in our previous paper.

2. EXPERIMENTAL PROCEDURE

The material used was bearing steel (modified JISSUJ2) similar to that used in our previous study,[61,62] and the chemical composition (in mass percentage) was as follows: 1.00 C, 0.31 Si, 0.45 Mn, 0.047 S, 1.52 Cr, 0.0075 Ca, and balance Fe. This bearing steel is not commercially available; however, since MnS inclusions have been reported to degrade RCF in bearing steels as mentioned above, this steel containing a high concentration of sulfur was fabricated in our laboratory so that crack initiation from MnS inclusions could be observed. Since MnS inclusions usually elongate in the hot rolling direction, calcium was added to the steel to obtain spheroidal MnS inclusions. A specimen 10 mm wide, 24 mm long, and 1 mm thick was cut from the forged bar. The specimens were quenched at 1103 K for 40 min and tempered at 453 K for 2 h. After tempering, the surfaces of the specimens were buffed and polished. The surface roughness of the specimen before RCF test was measures by laser microscopy was 0.0048 μm in arithmetic average roughness (*Ra*).

Table 1 shows the density and size of spheroidal and stringer-shaped inclusions measured by laminography, where density is defined by the number of inclusions in a 1 mm^3 volume. At a similar sulfur concentration, the number of inclusions is larger in the specimen with spheroidal inclusions than in the specimen with stringer-shaped inclusions. The diameters (length in radial direction) of spheroidal inclusions and stringer-shaped inclusions are almost the same; however, the length (length

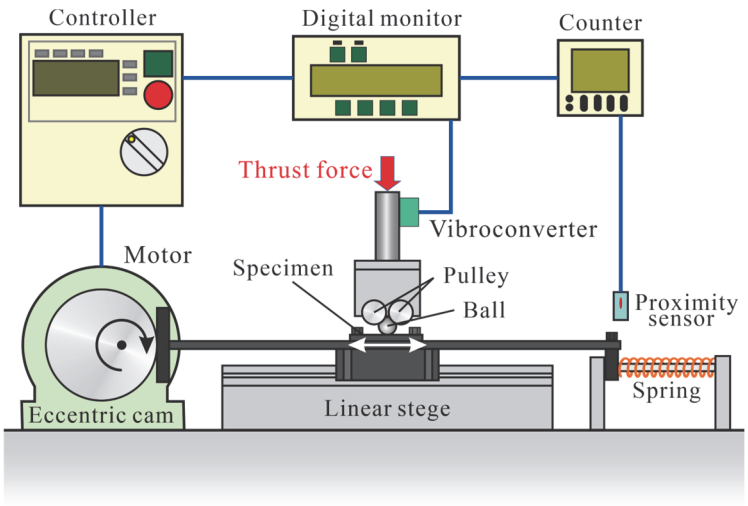

FIGURE 3 Rolling contact fatigue testing machine for laminography.[62]

in forged direction) and volume of the spheroidal inclusions are almost half and one-third those of the stringer-shaped inclusions, respectively. Compared with stringer-shaped inclusions, spheroidal inclusions show less scatter of length in both the forged and radial directions. The aspect ratio of spheroidal inclusions is 1.4 and extends in the forging direction, indicating that they are not completely spherical even after spheroidization.

Three types of RCF were performed, depending on the relative directions of forging and rolling, *i.e.*, the rolling surface is the crosssection of the forging bar for specimens with vertical inclusions and the longitudinal section of the forging bar for specimens with transversal and longitudinal inclusions, where the rolling direction for the specimens with transversal inclusions is radial direction, and that for the specimens with longitudinal inclusions is forging direction.

A special ball-on-disk RCF testing machine was developed as schematically illustrated in Figure 3, in which an eccentric cam with eccentric distance of 1.5 mm converts the rotary movement of the motor of 1,000 rpm to the reciprocal movement of the linear stage of 3.0 mm with frequency of 33.3 Hz, the vibroconverter detects flaking of the specimen, and the proximity sensor detects the edge of the linear stage to count the number of cycles. RCF tests were performed near the experimental hatch of the BL46XU beamline of the synchrotron radiation facility of Super Photon ring 8 GeV (SPring-8),[61,62] which uses an undulator beam and provides an X-ray beam with ultrabright high spatial coherence, enabling laminography with high spatial resolution in the micrometer range.[61,62] The RCF tests were conducted at the maximum Hertzian stress p_{max} of 5.39 GPa. According to Hertzian theory, under the present experimental conditions, the depth at which the shear stress is maximum in a plane parallel to the contact surface is 67 μm. This is sufficiently smaller than the thickness of the specimen, so the effect of the thickness on the flaking mechanism is considered to be small. In fact, the mechanism of flaking was similar to the present results for a specimen with a thickness of 5 mm, which was subjected to the same loading conditions.[28] Specimen was immersed in napthenic lubricant oil with a kinetic viscosity of 68.01 mm^2/s at 40 °C and 8.46 mm^2/s at 100 °C to reduce friction force. A linear extrapolation of these values to test temperature (24 °C) resulted in a value of 1 83.83 mm^2/s. The surface roughness of the specimen before and after flaking was measured by laser microscopy, and the film parameter, which represents the lubrication condition, was estimated. Since the surface roughness of the ball, however, could not be measured by laser microscopy, so it was assumed to be the same as that of specimen. The film parameter is 5.69 assuming that the contact area is circular before the formation of raceway. Assuming that the surface roughness does not change during the RCF test, the major axis length of the contact ellipse is the raceway width measured after flaking, and the minor axis length of the contact ellipse was calculated assuming that the contact area is the same value as that given by Hertz theory, the film parameter is 9.40. These values of film parameter indicates that the RCF tests were conducted under fluid lubrication condition. For reference, the film parameter calculated by the surface roughness, *R*a (0.0491 μm) measured after flaking is 1.29,

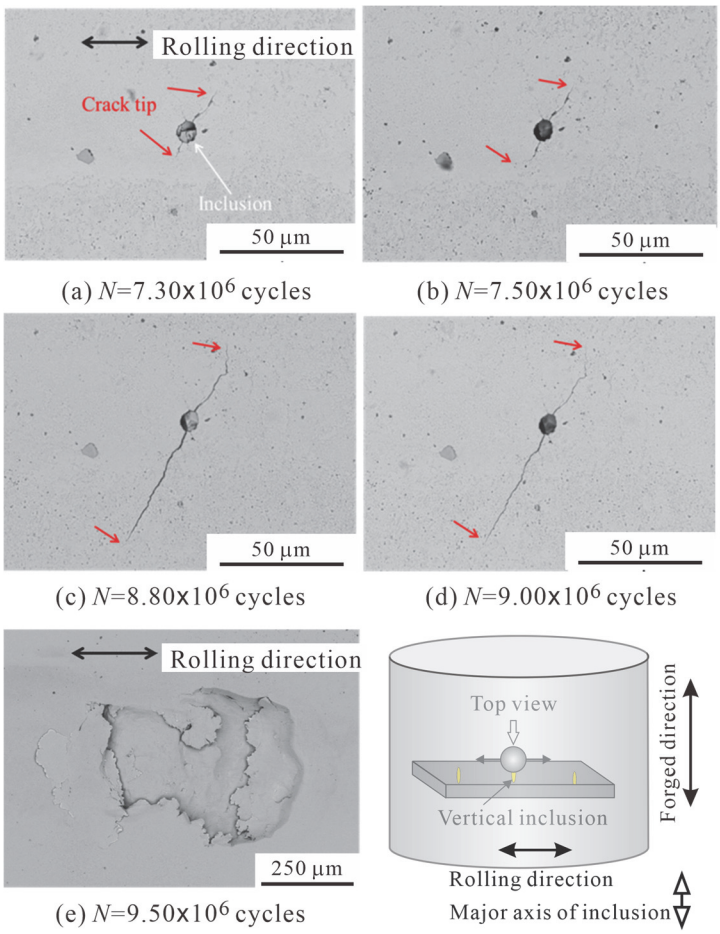

FIGURE 4 Crack initiation and propagation at surface observed by optical microscopy (Vertical inclusion).

where the surface roughness may have significantly increased due to ball vibration after flaking.

To observe crack initiation and propagation behaviors, tests were interrupted during the course of the RCF test, and surfaces were observed by optical microscopy or scanning electron microscopy (SEM), and three dimensional (3D) observations of the inside of specimens were conducted by laminography. The experimental setup and 3D reconstruction method have been described by Nakai et al. elsewhere. [41,42]

3. EXPERIMENTAL RESULTS

3.1 Vertical inclusions

3.1.1 Surface observation

Since the laminography findings indicated that RCF cracks always start from surface inclusions, surface observation can provide sufficient information about crack initiation.[28,41,42] Then, crack initiation and propagation behaviors on the same site on the specimen surface were observed sequentially. Figures 4a–4d show representative optical microscopy images and Figure 4e shows an

SEM image of crack profiles on the surface of a specimen with vertical inclusions.

The cracks initiated from the inclusions in the raceway and propagated toward the direction almost perpendicular to the rolling direction. Cracks always started from MnS inclusions because other types of inclusion such as Al_2O_3 and TiN, if existing, are much smaller than the MnS inclusions.

3.1.2 Laminography

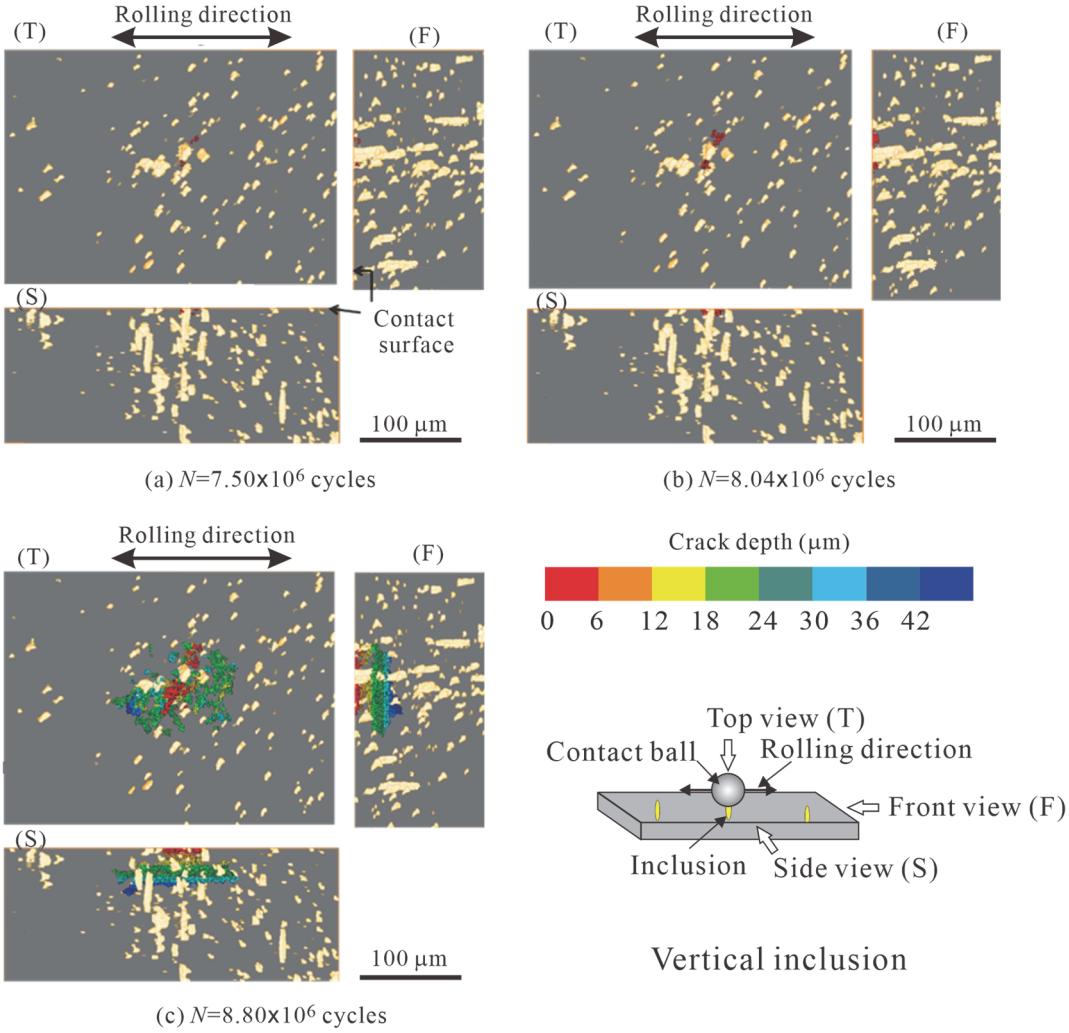

FIGURE 5 Laminography showing crack initiation from inclusion and propagation, where color code indicates distance from specimen surface (Vertical inclusion).

Figure 5 shows laminography images of inclusions and cracks, where (T), (F), and (S) indicate top, front, and side views, respectively. In these images, cracks are color-coded according to their depth from the surface, whereas inclusions are shown in pale yellow regardless of their depth. For Figure 5a, the number of cycles was the same as that for Figure 4a, where a small lateral crack, whose normal is perpendicular to the rolling direction, is observed. Inclusions may be dense or sparse depending on where they exist; however, cracks formed where inclusions are densely packed. Figure

4b was obtained at the number of cycles between Figures 4b and 3c, where the lateral crack propagates in the depth direction. Figure 4c was obtained at the same number of cycles as Figure 4c, where a crack parallel to the specimen surface (horizontal crack) is formed inside the specimen, whose depth is about 30 μm. This horizontal crack cannot be observed from the surface as shown in Figure 4c.

These laminography images indicate that in specimens with inclusions whose major axis is perpendicular to the specimen surface, cracks initiate from inclusions on the surface and propagate as lateral cracks. Subsequently, a horizontal crack parallel to the rolling surface forms and propagates inside the specimen, leading to flaking, indicating that the specimen with spheroidal vertical inclusions exhibits the same flaking formation mechanism as the specimen with stringer-shaped vertical inclusions,[41] *i.e.*, a crack is initiated on the surface.

3.2 Transversal inclusions

3.2.1 Surface observation

Figure 6 shows microscopy images of areas around the crack initiation site of a specimen with transversal inclusions. As shown in Figure 6a, cracks start forming at the longitudinal ends of an

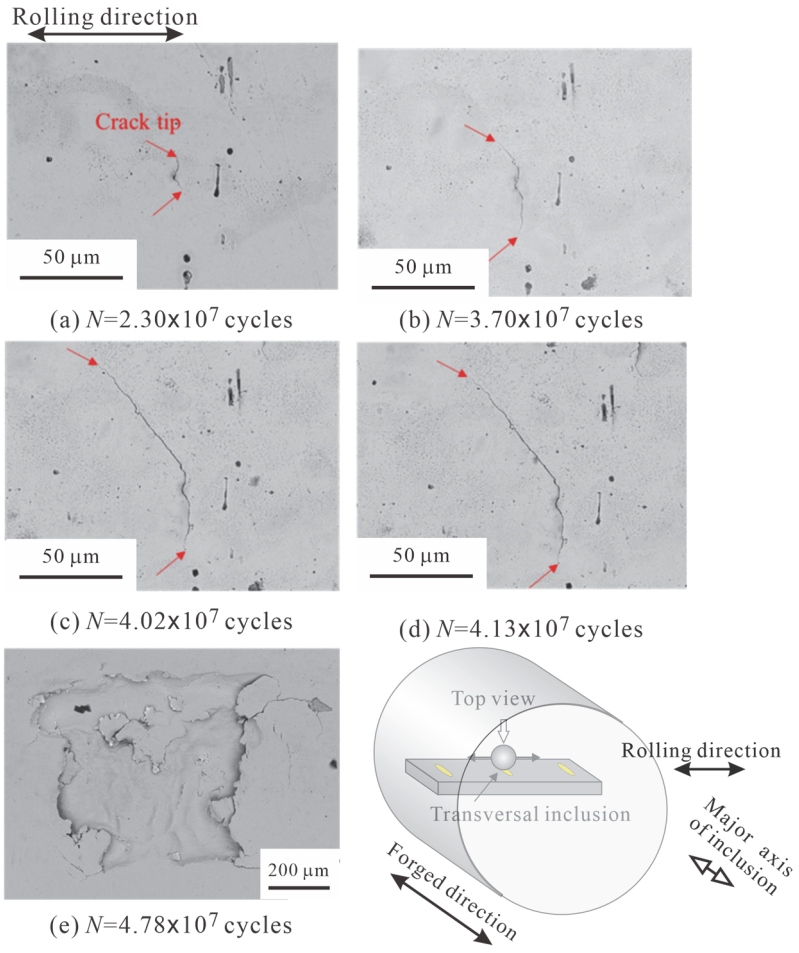

FIGURE 6 Crack initiation and propagation at surface observed by optical microscopy (Transversal inclusion).

inclusion on the surface where the stress concentration is highest, and propagate as shown in Figure 6b–6d. Finally, flaking occurred in the vicinity of these cracks as shown in Figure 6e. Therefore, the flaking mechanism in specimens with spheroidal transversal inclusions is similar to that in specimens with stringer-shaped transversal inclusions.[41]

3.2.2 Laminography

Laminography images of the RCF process in the specimen with transversal inclusions are shown

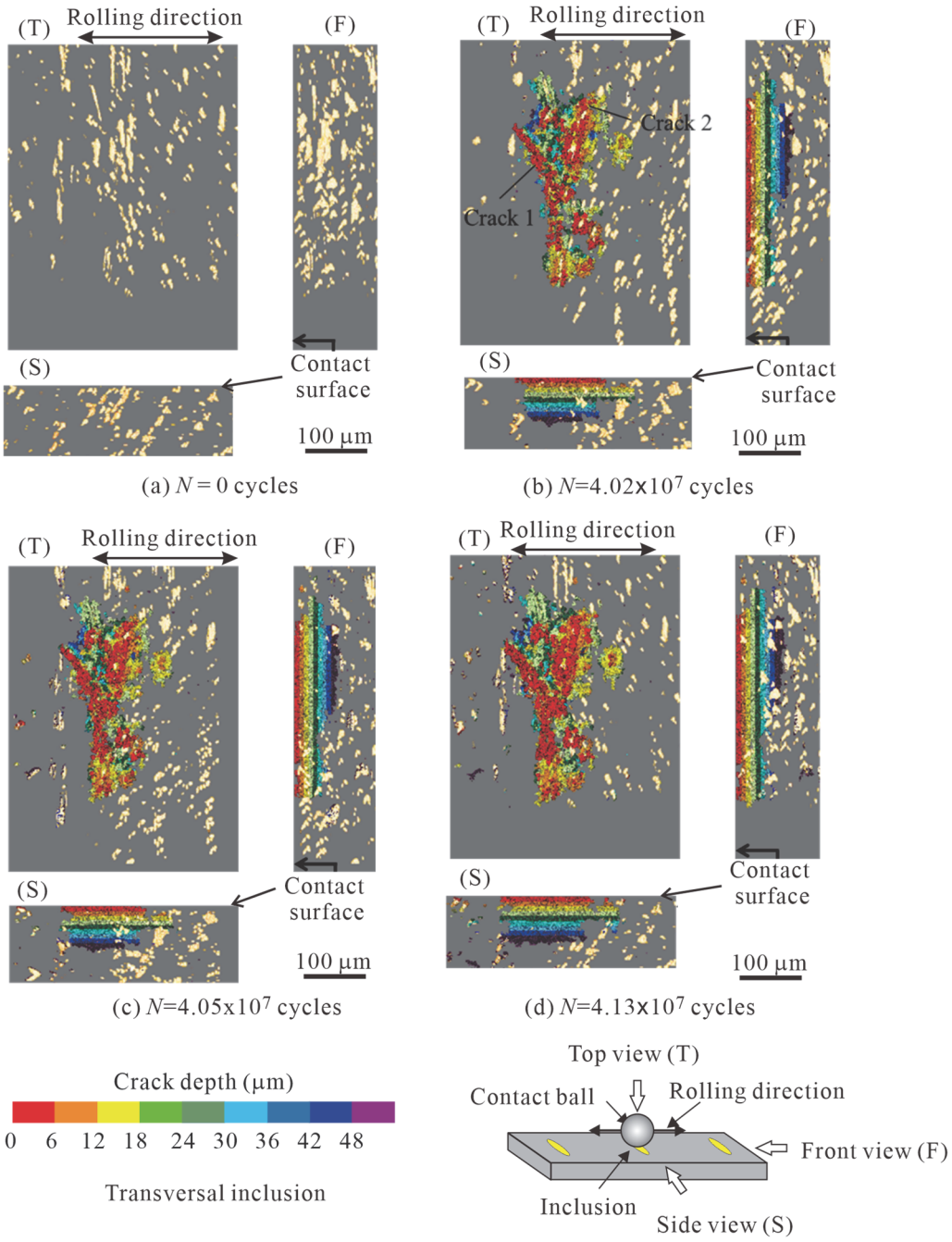

FIGURE 7 Laminography showing crack initiation from inclusion and propagation, where color code indicates distance from specimen surface (Transversal inclusion).

in Figure 7, where 7a was obtained before the RCF test, and only inclusions are indicated. Figure 6b was obtained at the same number of cycles as Figure 6c, Figure 7c was obtained at the number of cycles between Figure 6c and 5d, and Figure 7d was obtained at the same number of cycles as Figure 6d. In Figure 7b, two lateral cracks (indicated by Crack 1 and Crack 2) are formed, which have already grown to form a horizontal crack with a depth of about 30 μm, and they merged at the inner horizontal crack. Again, the cracks are considered to have formed on the surface where the inclusions are densely packed. Even in the case of a specimen with transversal inclusions, it is considered that lateral cracks formed first, then propagated in the depth direction to form horizontal cracks.

As seen in Figures 7c and 6d, the inner horizontal crack propagates almost parallel to the rolling surface, whereas Crack 2 propagates along the surface inclusions. As shown in Figure 6e, the horizontal crack propagation caused flaking. This process is similar to that observed in specimens with spheroidal vertical inclusions and in those with stringer-shaped transversal inclusions.[35]

3.3 Longitudinal inclusions

3.3.1 Surface observation

Figure 8 shows the microscopy images of areas around the crack initiation site of a specimen

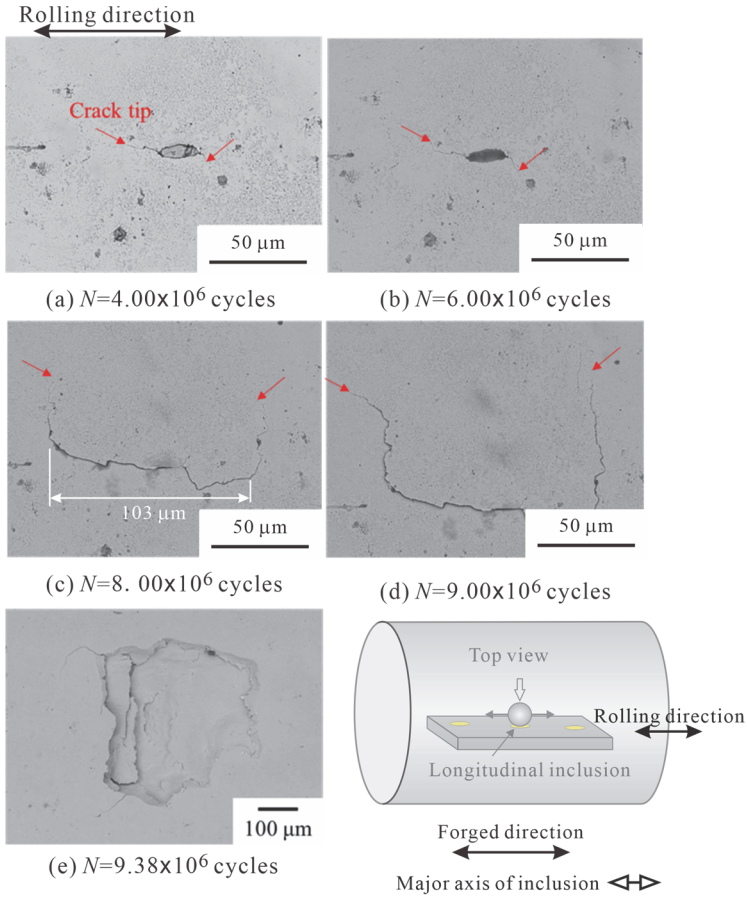

FIGURE 8 Crack initiation and propagation at surface observed by optical microscopy (Longitudinal inclusion).

with longitudinal inclusions. As shown in Figure 8a, longitudinal cracks started forming at the longitudinal ends of an inclusion, where the stress concentration is the highest, and Figure 8b propagated in the rolling direction to form longitudinal cracks. Figure 8c indicates that both tips of a longitudinal crack kinked to form lateral cracks when the surface length of the longitudinal crack reached 103 μm. This process is similar to that in specimens with stringer-shaped longitudinal inclusions,[62] where the kinking occurred when the surface length of a longitudinal crack reached approximately 100 μm, indicating that the condition to form lateral cracks from a longitudinal crack was not affected by the size and shape of inclusion at the crack initiation site. The condition to form lateral cracks must be controlled by mechanical factors, such as the stress intensity factor of a longitudinal crack. As shown in Figure 8e (at $N = 9.38\times10^6$ cycles), flaking occurred in the vicinity of the longitudinal crack initiation site.

3.3.2 Laminography

Figure 9 shows the laminography images of inclusions around the crack initiation site, where 9a shows the inclusions at the crack initiation site before the RCF test, and 9b was obtained immediately after the formation of a crack, where the number of cycles is the same as that for Figure 8a. In these images, cracks and inclusions are shown in red and pale yellow, respectively. Again, a longitudinal crack starts forming at a location where inclusions are densely packed. The depth of the crack is

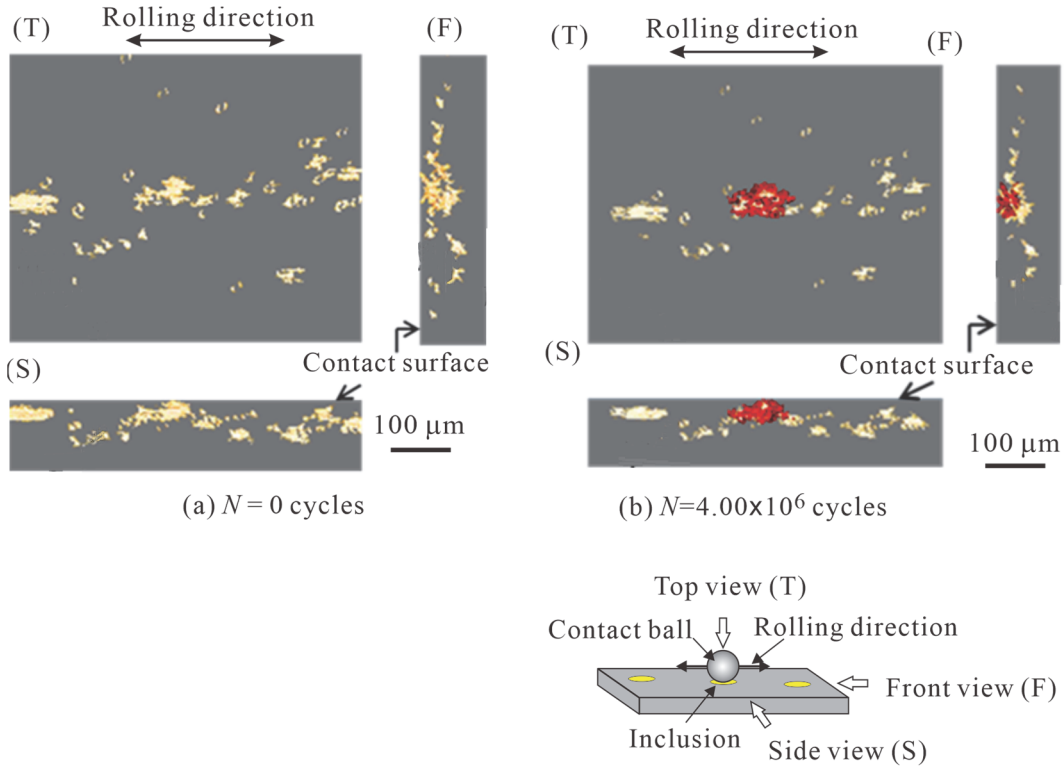

FIGURE 9 Laminography showing crack initiation from inclusion and propagation, where color code indicates distance from specimen surface (Longitudinal inclusion).

smaller than 30 μm, indicating that it was formed before the horizontal crack formation because the depth of horizontal crack was about 30 μm for specimens with vertical and transversal inclusions and the condition to form the horizontal crack is considered not to be affected by the shape and orientation of inclusions at the crack initiation site.

Since laminography could not be performed after the number of cycles shown in Figure 9b owing to the limited beam utilization time allowed us, we were unable to observe further the kinking and formation of horizontal crack; however, we did not find that the longitudinal cracks were formed before the formation of horizontal cracks. In specimens with stringer-shaped longitudinal inclusions, it has been shown that horizontal cracks initiate from the bottom of the lateral crack after kinking.[42] Since kinking should be independent of the shape and size of the inclusions at the crack initiation site, and it occurs far away from the inclusions at the crack initiation site, the behavior after kinking should be similar for specimens with stringer-shaped inclusions and those with spheroidal inclusions.

3.4 Effect of inclusion shape on flaking mechanism

As described in the previous section, the crack initiation mechanism differed between lateral and longitudinal inclusions, where lateral inclusions include both transversal and vertical inclusions; however, there is no significant difference in this mechanism between spheroidal and stringer-shaped inclusions in the same orientation. Although the crack propagation behavior in specimens with stringer-shaped inclusions was less affected by the existence of inclusions,[62] the crack propagation behavior in specimens with spheroidal inclusions was affected by the existence of inclusions around the cracks because the cracks initiated from the site where the inclusions were densely packed.

4. DISCUSSION

4.1 Crack initiation site

Figure 10 shows the crack initiation and flaking sites on the raceway as a function of distance from the center of the raceway, where the distances are normalized by half raceway width. Open symbols indicate the results for the spheroidal inclusions obtained in this study, and solid symbols indicate those for the stringer-shaped inclusions reported in our previous paper.[62] Figures 10a–10c show the location of each crack, and Figure 10d shows the average distances. Figure 10e shows the average distances from the center of flaking. These values are for the longitudinal crack initiation sites in specimens with longitudinal inclusions and the lateral crack initiation sites in specimens with lateral inclusions. The mechanical factors that control the crack initiation site to differ with respect to the inclusion orientation were discussed in our previous paper.[62]

The individual crack initiation sites shown in Figures 10a–10c are highly scattered; however, the average distances shown in Figure 10d tend to be closer to the edge of the raceway for spheroidal inclusions than for stringer-shaped inclusions. In addition, the crack initiation sites for specimens with vertical, transversal, and longitudinal inclusions are closer to the centerline in this order. As

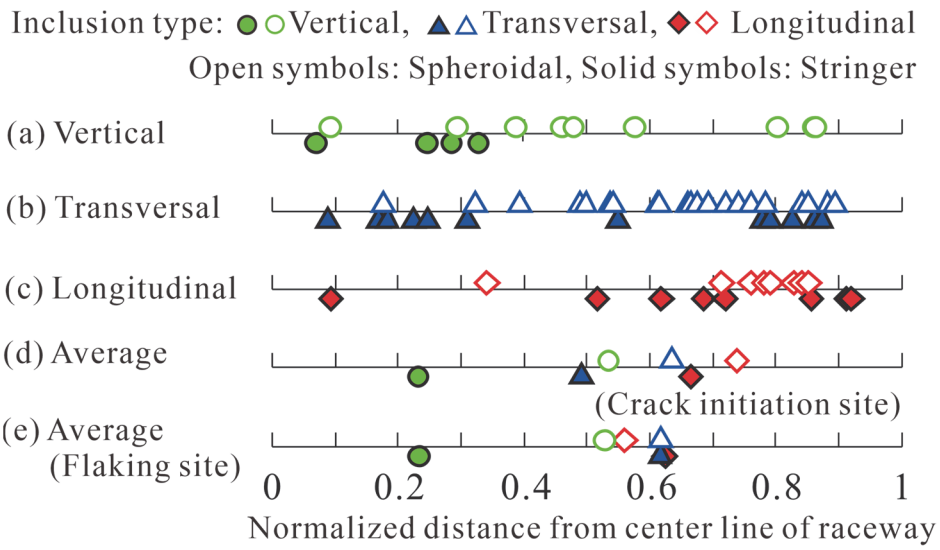

FIGURE 10 Distance between crack initiation site and center line of raceway, where distance is normalized by half of raceway width.

shown in Figure 10e, there is little difference in the distance from the flaking center except for the specimen with vertical stringer-shaped inclusions.

Figure 11 shows the effect of the standard deviation of inclusion size on the scatter of crack initiation sites shown in Figure 10, where the standard deviation is that for the major axis length of a transversal or longitudinal inclusion, and for the minor axis length of a vertical inclusion, indicating that the standard deviation of the crack initiation site is almost proportional to the standard deviation of the inclusion size except for specimens with spheroidal vertical inclusions. The effect of densely

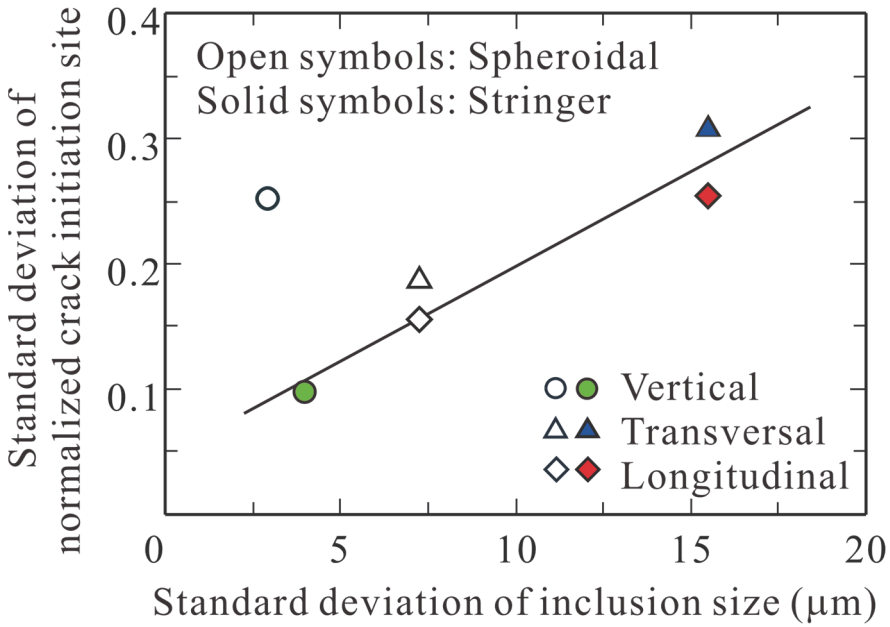

FIGURE 11 Effect of standard deviation of the inclusion size on scatter of crack initiation site.

packed inclusions around the crack initiation site may be responsible for this exception.

As reported in our previous paper, the crack initiation site is determined by the shear stress acting on the plane perpendicular to the specimen surface, containing the major axis of an inclusion. Since the axisymmetric stress field of the ball contact to the specimen surface, the antiplane shear stress is maximum at the edge of the raceway for longitudinal inclusions and at the center of the ball for lateral inclusions.[62]

The driving force for crack initiation is the product of local stress and the stress concentration due to inclusions, where the scatter of the size of the inclusions changes the stress concentration and thus the crack initiation point.

4.2 Statistical analysis

Since the flaking life in bearing steel is controlled by the weakest part of the material, the flaking life distribution follows the Weibull distribution.[48] In the original Weibull distribution, the cumulative distribution function $F(N_f)$ has three parameters, and is expressed as:[63]

$$F\left(N_f\right) = 1 - \exp\left[-\left(\frac{N_f - \gamma}{\beta}\right)^{\alpha}\right], \quad (1)$$

where N_f is the number of cycles to flaking, α is the shape parameter, β is the scale parameter, and γ is the location parameter. The smaller the shape parameter α, the more spread out the distribution, the larger the scale parameter β, the longer the life, and γ is the number of cycles at $F(N_f) = 0$.[64] Although the two-parameter Weibull distribution, which ignores the positional population ($\gamma = 0$) and simplifies the calculation, is becoming popular, it is generally necessary to consider the three-parameter Weibull distribution including the positional population in the long-life region near the fatigue limit.[65-67] Then, the flaking life of RCF is examined by applying the three-parameter Weibull distribution concept. In the case of the original equation based on a three-parameter Weibull distribution, it is not easy to estimate γ. In this paper, these three parameters are obtained by the correlation coefficient method proposed by Sakai and Tanaka.[65]

The cumulative failure probability $F(x_i)$ of the i_{th} datum x_i at the ordinate is calculated as:

$$F\left(x_i\right) = i - \frac{0.3}{n + 0.4}, \quad (2)$$

where n is the total number of specimens tested at the same Hertz stress.

The Weibull plot of the flaking life is shown in Figure 12, where 12a shows the effect of the orientation of spheroidal inclusions, and Figures12b–12d show the effect of inclusion shape in each orientation. Symbols with arrows in these figures represent specimens on which the RCF test was terminated before flaking. As shown in Figure 12a, for spheroidal inclusions, the scatter of flaking life is smallest for specimens with vertical inclusions and largest for specimens with longitudinal inclusions. The average flaking life ($F(N_f)$=50) is slightly shorter for specimens with vertical

322 inclusions than for those with transversal inclusions; however, it is about 10 times longer for
323 specimens with longitudinal inclusions because the flaking life of specimens with longitudinal

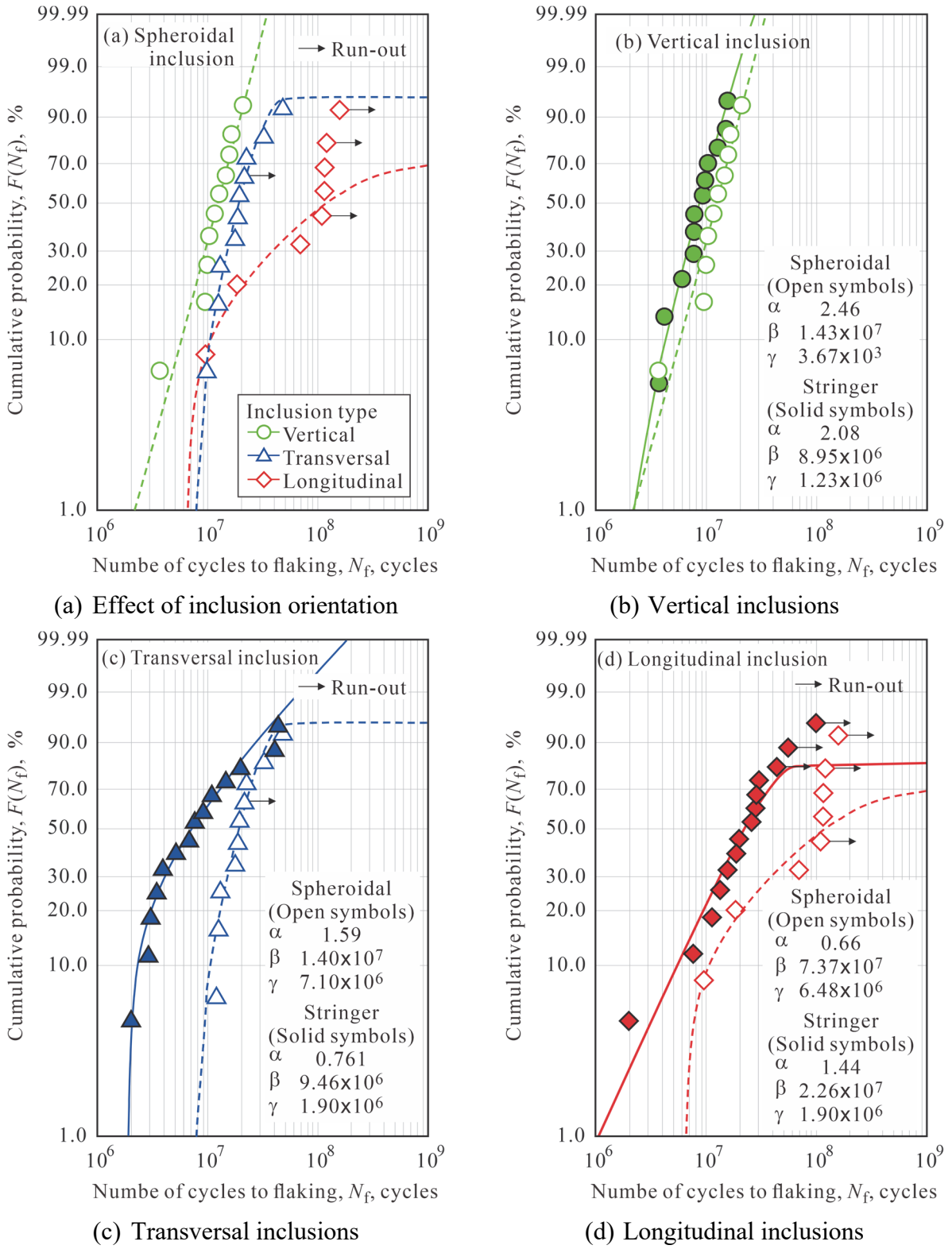

(a) Effect of inclusion orientation (b) Vertical inclusions

(c) Transversal inclusions (d) Longitudinal inclusions

FIGURE 12 Weibull plot of the flaking life of the rolling contact fatigue for spheroidal inclusions, where (a) compares the rolling directions for spheroidal inclusions, and (b)-(d) compare the results for spheroidal and stringer-shaped inclusions in each inclusion orientation. Symbols with arrows in the figure represent specimens for which the test was terminated before flaking.

inclusions increased because of the increased crack propagation life in the rolling direction.

Alley and Neu analyzed the effect of the orientation of lateral inclusions on RCF strength on the basis of the stress under the surface, which was calculated by finite element analysis.[43] They concluded that RCF strength is highest for vertical inclusions. Allison and Pandkar evaluated the RCF limit of longitudinal and lateral inclusions by finite element analysis, and they concluded that the effects of the inclusion orientation and geometry on the RCF limit were minor.[44] The results obtained by finite element analysis do not agree with our experimental results.

For fatigue, the stress amplitude is the most influential factor. This is the reason why the discussion based on the maximum stress obtained by the finite element analysis do not agree with our experimental results. The authors reported that the effect of inclusion orientation on the crack path in RCF behavior could be explained in terms of antiplane shear stress amplitude acting on inclusions, *i.e.*, longitudinal inclusions received pulsated cyclic stress, whereas the lateral inclusions received alternating cyclic stress, indicating that the antiplane shear stress amplitude on longitudinal inclusions was half that on lateral inclusions whereas the maximum stresses on those inclusions are identical.[62] As a result, formation of the longitudinal crack proceeds the formation of lateral cracks in the RCF process of specimens with longitudinal inclusions, whereas lateral cracks formed without formation of longitudinal cracks in specimens with lateral inclusions. Not only mechanical factors but also wear is important in longitudinal crack initiation from longitudinal inclusions.

The effect of inclusion shape is shown in Figures 12b–12d. The scale parameter β, which represents the flaking life, is larger for specimens with spheroidal inclusions than for specimens with stringer-shaped inclusions for all orientations. This is due to the lower stress concentration in the spheroidal inclusions than in the stringer-shaped inclusions. The shape parameter α, which represents the scatter, is larger for specimen with spheroidal inclusions than for specimen with stringer-shaped vertical and transversal inclusions, indicating that specimen with spheroidal inclusions show less scatter than for specimen with stringer-shaped inclusions. However, specimen with spheroidal longitudinal inclusions has a smaller α than for specimen with stringer-shaped inclusions, indicating that the scatter is larger. This is related to the scatter of inclusion size, which will be discussed in detail later.

4.3 Crack initiation and propagation lives

Figure 13 shows the average flaking life N_f divided into surface crack initiation life N_i and crack propagation life N_p. Although the flaking life of specimens with spheroidal inclusions is longer than that of specimens with stringer-shaped inclusions regardless of the inclusion orientation, the effect of inclusion shape on N_f differs between specimens with spheroidal and stringer-shaped inclusions, *i.e.*, the N_f for specimens with spheroidal vertical inclusions is shorter than that for specimens with spheroidal transversal inclusions, whereas the N_f for specimens with stringer-shaped vertical inclusions is almost the same as that for specimens with stringer-shaped transversal inclusions. For

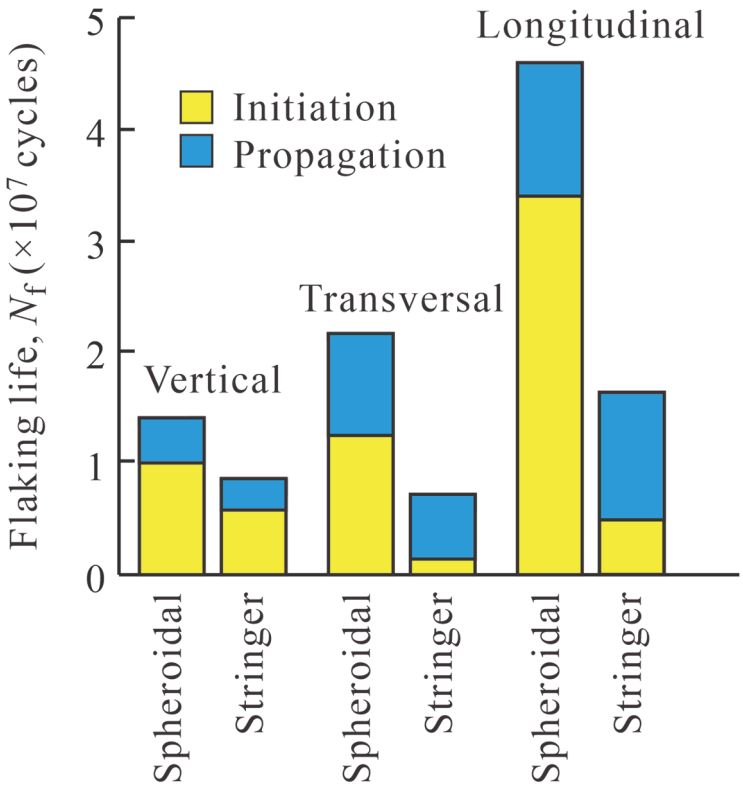

FIGURE 13 Flaking life divided into surface crack initiation life and crack propagation life.

either shape, the N_f for specimens with longitudinal inclusions is the longest.

The crack initiation lives of the specimens with spheroidal vertical and transversal inclusions are almost the same, whereas specimens with stringer-shaped vertical inclusions have a longer crack initiation life than the stringer-shaped transversal inclusion specimens. The crack initiation life of the specimens with spheroidal vertical inclusions was almost the same as that of the specimens with spheroidal transversal inclusions. This is because the difference in stress concentration due to the difference in orientation is smaller for the spheroidal inclusions than for the stringer-shaped inclusions.

For either inclusion shape, the crack propagation life was shorter for specimens with spheroidal inclusions than for specimens with stringer-shaped inclusions. The higher density of inclusions may account for this difference, as cracks tend to propagate along the interface between the inclusions and the matrix.

Figure_14a shows the effect of the length of an inclusion at the surface l on the crack initiation life N_i, and Figure 14b shows the effect of the depth of an inclusion d on the crack propagation life N_p, where l in Figure 14a is the major axis length of a transversal or longitudinal inclusion, and the minor axis length of a vertical inclusion. d in Figure 14b is the minor axis length of a transversal or longitudinal inclusion and the major axis length of a vertical inclusion. In Figure 14a, N_i decreases with l, and this trend is almost the same for specimens with lateral inclusions where the rolling direction and the major axis of the inclusion are perpendicular. On the other hand, N_i for longitudinal

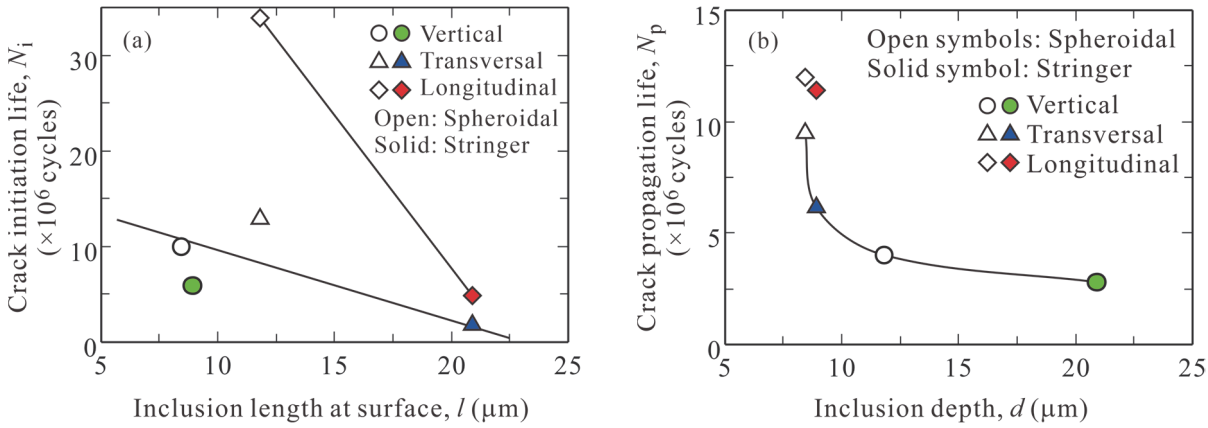

(a) Crack initiation life vs. surface initiation length. (b) Crack propagation life vs. inclusion depth.

FIGURE 14 Effect of inclusion size on crack initiation and propagation lives.

inclusions, where the major axis of the inclusion is parallel to the rolling direction, is longer than N_i for specimens with lateral inclusions. This is because, as described in the previous paper, the maximum shear stress perpendicular to the rolling plane including the major axis of the inclusion is independent of the inclusion direction; however, its amplitude is twofold for lateral inclusions compared with that for longitudinal inclusions.

In Figure 14b, N_p decreases with d, and this trend is the same for specimens with lateral inclusions, where the crack propagates toward the direction perpendicular to the rolling direction immediately after crack initiation. In the case of longitudinal inclusions, the crack propagates toward the rolling direction and then propagates vertically, resulting in a longer crack propagation life for N_p. Since the horizontal cracks propagate inside the specimen away from the crack initiation point,[62] the

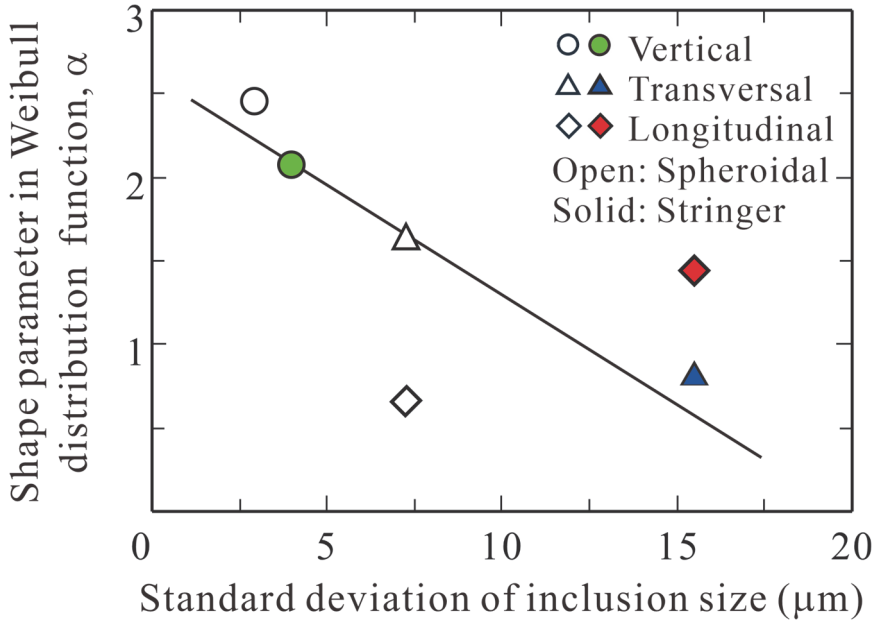

FIGURE 15 Effect of standard deviation of inclusion size on scatter of flaking life.

horizontal crack propagation life is the same for all inclusion shapes and sizes. Therefore, the difference in crack propagation life is attributed to the difference in the propagation life of a crack perpendicular to the rolling surface. Then, by measuring the length and depth of the inclusion, the flaking life can be predicted from the relationships shown in Figure 14.

Figure 15 shows the effect of the standard deviation of inclusion size on the coefficient of Weibull distribution function α, where the definition of the standard deviation is the same as that employed in Figure 11. The scatter of flaking life is larger for a smaller α, indicating that the flaking life also varies with the scatter of inclusion dimensions. Although the flaking life is the sum of the crack initiation life and the crack propagation life, similar results can be obtained using the standard deviation of either size, the major, or minor axis because the standard deviations of the major-axis and minor-axis sizes of inclusions are almost proportional to each other, as shown in Table 1.

5. CONCLUSIONS

In this study, RCF tests were conducted on specimens containing spheroidal inclusions, and the size of inclusions and the crack initiation point were investigated by laminography using ultrabright synchrotron radiation X-rays, and the crack propagation behavior up to flaking was clarified. The results were compared with those of specimens containing stringer-shaped inclusions to clarify the effect of inclusion shape on the RCF mechanism and life. The results obtained are as follows.

1. The crack initiation and propagation mechanisms in the specimens with spheroidal and stringer-shaped inclusions were similar. For specimens with longitudinal inclusions, surface cracks started forming at their tips. After the cracks propagated toward the rolling direction, a longitudinal crack was kinked simultaneously at both its tips, and propagated toward the direction perpendicular to the rolling direction to form lateral cracks. After kinking, horizontal cracks were formed from the deepest point of a lateral crack, leading to flaking. On the other hand, for specimens with lateral inclusions, surface cracks propagated toward the lateral direction without the formation of longitudinal cracks. The subsequent behavior was similar to that of specimens with longitudinal inclusions.
2. The flaking life of the specimens with spheroid inclusions was longer than that of the specimens with stringer-shaped inclusions. In particular, the life up to vertical crack initiation on the specimen surface was found to be affected by the inclusion shape.
3. The surface crack initiation life was shorter for specimens with longer inclusions at the surface. This observation was similar for specimens with vertical and transversal inclusions; however, specimens with longitudinal inclusions had a longer life.
4. The crack propagation life decreased with increasing depth of the inclusion. This trend was almost the same for specimens with vertical and transversal inclusions; however, specimens with longitudinal inclusions had a longer life than specimens with lateral inclusions.
5. The greater the scatter of inclusion size, the greater the scatter of the crack initiation point and

flaking life.

ACKNOWLEDGMENT

The synchrotron radiation experiments were performed at beam line BL46XU of SPring-8 with the approval of the Japan Synchrotron Radiation Research Institute (JASRI) under proposal numbers 2018A1548, 2018B1612, 2019A1635, 2019B1693,2020A1620. The authors are grateful for the technical support of Dr. K. Kajiwara (JASRI).

CONFLICT OF INTEREST

The authors declare that they have no conflict of interest.

AUTHOR CONTRIBUTIONS

Y. Nakai, D. Shiozawa, S. Kikuchi, T. Makino, and Y. Neishi conceived of the presented idea. T. Makino and Y. Neishi contributed to sample preparation. T. Nishina, H. Kobayashi, and M. Kurahashi carried out the experiment. All authors contributed to the interpretation of the results. Y. Nakai, D. Shiozawa, S. Kikuchi, T. Makino, and Y. Neishi contributed to the final manuscript.

REFERENCES

1. Makino T, Kato T, Hirakawa K. The effect of slip ratio on the rolling contact fatigue property of railway wheel steel. Int J Fatigue. 2012;36:68-79.
2. Horimoto M, Makino T, Matsumoto H. The effect of slip conditions on the contact fatigue strength for pitting of a carburized steel. Solid State Phenom. 2006;118:521-526.
3. Meyler D, Magel E, Kalousek J. Reducing operating costs through improved wheel performance. 13th Int Wheelset Cong. 2001;CD-ROM.
4. Šraml M, Flašker J, Potrč I. Numerical procedure for predicting the rolling contact fatigue crack initiation. Int J Fatigue. 2003;25:585-595.
5. Hiraoka K, Nagao M, Isomoto T. Study on flaking process in bearings by white etching area generation. ASTM STP 1465. 2007;234-240.
6. Gustaf L, Palmgren A. Dynamic capacity of rolling bearings. J Appl Mech, Trans ASME. 1949;16:165-172.
7. Styri H. Fatigue strength of ball bearing races and heat-treated 52100 steel specimens. Proc ASTM. 1951;51:682–700.
8. Donzella G, Petrogalli C. A failure assessment diagram for components subjected to rolling contact loading. Int J Fatigue. 2010;32:256-268.
9. El Laithy M, Wang L, Harvey TJ, Vierneusel B. Further understanding of rolling contact fatigue in rolling element bearings-a review. Tribology Int. 2018;140:105849.
10. Keer LM, Bryant MD. A pitting model for rolling contact fatigue. J Lub Trib, Trans ASME. 1983;105:198-205.

11. Hannes D, Alfredsson B. Rolling contact fatigue crack path prediction by the asperity point load mechanism. Eng Fract Mech. 2011;78:2848-2869.
12. Ringsberg JW, Loo-Morrey M, Josefson BL. Prediction of fatigue crack initiation for rolling contact fatigue. Int J Fatigue. 2000;22:205-215.
13. Ringsberg JW. Life prediction of rolling contact fatigue crack initiation. Int J Fatigue. 2001;23:575-586.
14. Ghaffari MA, Zhang Y, Xiao S. Multiscale modeling and simulation of rolling contact fatigue. Int J Fatigue. 2018;108:9-17.
15. Kanetani K, Ushioda K. Mechanism of white band (WB) formation due to rolling contact fatigue in carburized SAE4320 steel. Mater Trans. 2020;61:1750-1759.
16. Swahn H, Becker PC , Vingsbo O. Martensite decay during rolling contact fatigue in ball bearings. Metarru Trans. 1976;7A:1099-1110.
17. Šmeļova V, Schwedt A, Wang L, Holweger W, Mayer J. Microstructural changes in white etching cracks (WECs) and their relationship with those in dark etching region (DER) and white etching bands (WEBs) due to rolling contact fatigue (RCF). Int J Fatigue. 2017;100:148-158.
18. Li S, Wu J, Petrov RH, Li Z, Dollevoet R, Sietsma J. “Brown etching layer”: A possible new insight into the crack initiation of rolling contact fatigue in rail steels?. Eng Fail Anal. 2016;66:8-18.
19. Li SX, Su YS, Shu XD, Chen JJ. Microstructural evolution in bearing steel under rolling contact fatigue. Wear. 2017;380-381:146-153.
20. Evans MH, Walker JC, Ma C, Wang L, Wood RJK. A FIB/TEM study of butterfly crack formation and white etching area (WEA) microstructural changes under rolling contact fatigue in 100Cr6 bearing steel. Mater Sci Eng: A. 2013;570:127-134.
21. Morris D, Sadeghi F. Retained austenite stability on rolling contact fatigue performance of 8620 case-carburized steel. Fatigue Fract Eng Mat Struct: 2022; 45: 55-68.
22. Shi Z, Wang H, Gao Y, Wang Y, Yu F, Xu H, Zhang X, Shang C, Cao W. Improve fatigue and mechanical properties of high carbon bearing steel by a new double vacuum melting route. Fatigue Fract Eng Mat Struct: 2022; 45:1995-2009.
23. Su YS, Li SX, Yu F, Lu SY, Wang YG. Revealing the shear band origin of white etching area in rolling contact fatigue of bearing steel. Int J Fatigue. 2021;142:105929.
24. Grabulov A, Ziese U, Zandbergen HW. TEM/SEM investigation of microstructural changes within the white etching area under rolling contact fatigue and 3-D crack reconstruction by focused ion beam. Scripta Mater. 2007;57:635-638.
25. Martin JA, Borgese SF, Eberhardt AD. Microstructural alterations of rolling bearing steel undergoing cyclic stressing. J Basic Eng Trans ASME. 1966;88:555-565.
26. Sugino K, Miyamoto K, Nagumo M, Aoko K. Structural alterations of bearing steels under rolling contact fatigue. Trans ISIJ. 1970;10:98-111.

27. Becker PC. Microstructural changes around non-metallic inclusions caused by rolling-contact fatigue of ball-bearing steels. Metals Tech. 1981;234-243.
28. Makino T, Neishi Y, Shiozawa D, Fukuda Y, Kajiwara K, Nakai Y. Evaluation of rolling contact fatigue crack path in high strength steel with artificial defects. Int J Fatigue. 2014;68:168-177.
29. Chen Q, Shao E, Zhao D, Guo J, Fan Z. Measurement of the critical size of inclusions initiating contact fatigue cracks and its application in bearing steel. Wear. 1991;147:285-294.
30. Nagao M, Hiraoka K, Unigame Y. Influence of nonmetallic inclusion size on rolling contact fatigue life in bearing steel. Sanyo Tech Report. 2005;12:38-45.
31. Kerrigan A, Kuijpers JC, Gabelli A, Ioannides E. Cleanliness of bearing steels and fatigue life of rolling contacts. ASTM STP 1465. 2007;101-106.
32. Unigame Y, Hiraoka K, Takasu I, Kato Y. Evaluation procedures of nonmetallic inclusions in steel for highly reliable bearings. J ASTM Int. 2007;3:34-41.
33. Hashimoto K, Fujimatsu T, Tsunekage N, Hiraoka K, Kida K. Effect of inclusion/matrix interface cavities on internal-fracture-type rolling contact fatigue life. Mater Des. 2011;32:4980-4985.
34. Lewis MWJ, Tomkins B. A fracture mechanics interpretation of rolling bearing fatigue, proceedings of the institution of mechanical engineers, Part J. J Eng Tribol. 2012;226:389-405.
35. Neishi Y, Makino T, Matsui N, Matsumoto H, Higashida M, Ambai H. Influence of the inclusion shape on the rolling contact fatigue life of carburized steels. Metall Mater Trans A. 2013;44:2131-2139.
36. Tsuchida T, Tamura E. Mechanism of crack initiation at non-metallic inclusion under rolling contact fatigue in bearing steels. Kobe Steel Eng Reports. 2011;61:62-65.
37. Stiénon A, Fazekas A, Buffiere J-Y, Vincent A, Daguier P, Merchi F. A new methodology based on X-ray micro-tomography to estimate stress concentrations around inclusions in high strength steels. Materials Sci Eng A. 2009;513-4:376-383.
38. Stiénon A, Fazekas A, Buffiere J-Y, Daguier P, Merchi F, Vincent A. A new methodology for predicting fatigue properties of bearing steels: from X-ray micro-tomography and ultrasonic measurements to the bearing lives distribution. J ASTM Int. 2010;7:1-14.
39. Shiozawa D, Makino T, Neishi Y, Nakai Y. Observation of rolling contact fatigue cracks by laminography using ultra-bright synchrotron radiation. Procedia Mat Sci. 2014;3:159-164.
40. Nakai Y, Shiozawa D , Kikuchi S , Sato K, Obama T, Makino T, Neishi Y. In situ observation of rolling contact fatigue cracks by laminography using ultra-bright synchrotron radiation. Frattura Integ Stru. 2014;34:267-275.
41. Nakai Y, Shiozawa D, Kikuchi S, Obama T, Saito H, Makino T, Neishi Y. 4D observations of rolling contact fatigue processes by laminography using ultra-bright synchrotron radiation. Eng Fract Mech. 2017;183:180-189.

42. Nakai Y, Shiozawa D, Kurimura T, Kajiwara K. Observation of fretting fatigue cracks by micro computed-tomography using ultrabright synchrotron radiation. Proc SPIE. 2010;7522:75224B: 1-7.
43. Alley ES, Neu RW. Microstructure-sensitive modeling of rolling contact fatigue. Int J Fatigue. 2010;32:841-850.
44. Allison B, Pandkar A. Critical factors for determining a first estimate of fatigue limit of bearing steels under rolling contact fatigue. Int J Fatigue. 2018;117:396-406.
45. Shen Y, Mobasher S, Sadeghi MF, Paulson K, Trice RW. Effect of retained austenite – Compressive residual stresses on rolling contact fatigue life of carburized AISI 8620 steel. Int J Fatigue. 2015; 5:135-144.
46. Walvekar AA, Sadeghi F. Rolling contact fatigue of case carburized steels. Int J Fatigue. 2017;95:264-281.
47. Golmohammadi Z, Walvekar A, Sadeghi F. A 3D efficient finite element model to simulate rolling contact fatigue under high loading conditions. Tribology Int. 2018;126:258-269.
48. Zhao YX, Liu HB. Weibull modeling of the probabilistic S–N curves for rolling contact fatigue. Int J Fatigue. 2014;66:47-54.
49. Vijay A, Paulson N, Sadeghi F. A 3D finite element modelling of crystalline anisotropy in rolling contact fatigue. Int J Fatigue. 2018;106:92-102.
50. Naeimi M, Li Z, Qian Z, Zhou Y, Wu J, Petrov RH, Sietsma J, Dollevoet R. Reconstruction of the rolling contact fatigue cracks in rails using X-ray computed tomography. NDT E Int. 2017;92:199-212.
51. Jessop C, Ahlstrom J, Hammar L, Faster S. 3D characterization of rolling contact fatigue crack networks. Wear. 2016;366-7:392-400.
52. Shiozawa D, Nakai Y, Kurimura T, Morikage Y, Tanaka H, Okado H, Miyashita T, Kajiwara K. Observation of cracks in steels using synchrotron radiation X-ray micro tomography. J Soc Mater Sci Jpn. 2007;56:951-957.
53. Yoshinaka F, Nakamura T, Nakayama S, Shiozawa D, Nakai Y, Uesugi K. Non-destructive observation of internal fatigue crack growth in Ti-6Al-4V by using synchrotron radiation μCT imaging. Int J Fatigue. 2016;93:397-405.
54. Xue G, Tomoda Y, Nakamura T, Fujimura N, Takahashi K, Yoshinaka F, Takeuchi A, Uesugi M, Uesugi K. Detection of small internal fatigue cracks in Ti-6Al-4V via synchrotron radiation nanocomputed tomography. Fatigue Fract Eng Mat Struct: 2022; 45: 2693-2702.
55. Shiozawa D, Nakai Y, Murakami T, Nosho H. Observation of 3D shape and propagation mode transition of fatigue cracks in Ti-6Al-4V under cyclic torsion using CT imaging with ultra-bright synchrotron radiation. Int J Fatigue. 2014;58:158-165.
56. Shiozawa, D, Nakai, Y, Miura, R, Masada, N, Matsuda, S, Nakao, R, 4D evaluation of grain shape and fatigue damage of individual grains in polycrystalline alloys by diffraction contrast tomography using ultrabright synchrotron radiation, Int J Fatigue. 2016;82:247-255.

57. Nakai Y, Shiozawa D, Asakawa N, Nonaka K, Kikuchi S. Change of misorientation of individual grains in fatigue of polycrystalline alloys by diffraction contrast tomography using ultrabright synchrotron radiation. Structural Integrity Procedia. 2017;3:402-410.
58. Makino T, Neishi Y, Shiozawa D, Kikuchi S, Okada T, Kajiwara K, Nakai Y. Effect of defect shape on rolling contact fatigue crack initiation and propagation in high strength steel. Int J Fatigue. 2016;92:507-516.
59. Makino T, Neishi Y, Shiozawa D, Kikuchi S, Saito H, Kajiwara K, Nakai Y. Rolling contact fatigue damage from artificial defects and sulphide inclusions in high strength steel. Procedia Struct Integ. 2017;7:468-475.
60. Makino T, Neishi Y, Shiozawa D, Kikuchi S, Okada S, Kajiwara K, Nakai Y. Effect of defect length on rolling contact fatigue crack propagation in high strength steel. Frattura Integ Stru. 2015;34:379-386.
61. Nakai Y, Shiozawa D, Kikuchi S, Obama T, Saito H, Makino T, Neishi Y. Effects of inclusion size and orientation on rolling contact fatigue crack initiation observed by laminography using ultra-bright synchrotron radiation. Procedia Struct Integ. 2016;2:3117-3124.
62. Nakai Y., Shiozawa D, Kikuchi S, Saito H, Nishina T, Kobayashi H, Makino T, Neishi Y, Inclusion orientation dependent flaking process in rolling contact fatigue observed by laminography using ultrabright synchrotron radiation X-ray. Fatigue Fract Eng Mat Struct: 2022;45:2200-2214.
63. Weibull W. A statistical distribution function of wide applicability. J Appl Mech. 1951; 18: 293–297.
64. Kikuchi S, Kubozono H, Nukui Y, Nakai Y, Ueno A, Kawabata MO, Ameyama K. Statistical fatigue properties and small fatigue crack propagation in bimodal harmonic structured Ti-6Al-4V alloy under four-point bending. Mater Sci Eng A. 2018;711:29-36.
65. Sakai T, Tanaka T, Estimation of three parameters of Weibull distribution in relation to parameter estimation of fatigue life distribution (Continued Report). J. Soc. Mat. Sci., Jpn. 1980; 29: 17-23.
66. Schijve J. Statistical distribution functions and fatigue of structures. Int J Fatigue. 2005;27:1031–1039.
67. Strzelecki P. Determination of fatigue life for low probability of failure for different stress levels using 3-parameter Weibull distribution. Int. J. Fatigue; 2021;145:106080.